The role of damped Alfvén waves on magnetospheric accretion models of young stars

M. J. Vasconcelos

Departamento de Ciências Exatas e Tecnológicas, Universidade Estadual de Santa Cruz
Rodovia Ilhéus - Itabuna, km. 16, 45650-000 Ilhéus, BA, BRAZIL

mjvasc@uesc.br

and

V. Jatenco-Pereira and R. Opher

Instituto de Astronomia, Geofísica e Ciências Atmosféricas
Universidade de São Paulo
Av. Miguel Stéfano 4200, 04301-904 São Paulo, SP, BRAZIL

ABSTRACT

We examine the role of Alfvén wave damping in heating the plasma in the magnetic funnels of magnetospheric accretion models of young stars. We study four different damping mechanisms of the Alfvén waves: nonlinear, turbulent, viscous-resistive and collisional. Two different possible origins for the Alfvén waves are discussed: 1) Alfvén waves generated at the surface of the star by the shock produced by the infalling matter; and 2) Alfvén waves generated locally in the funnel by the Kelvin-Helmholtz instability. We find that, in general, the damping lengths are smaller than the tube length. Since thermal conduction in the tube is not efficient, Alfvén waves generated only at the star's surface cannot heat the tube to the temperatures necessary to fit the observations. Only for very low frequency Alfvén waves $\sim 10^{-5}$ the ion cyclotron frequency, is the viscous-resistive damping length greater than the tube length. In this case, the Alfvén waves produced at the surface of the star are able to heat the whole tube. Otherwise, local production of Alfvén waves is required to explain the observations. The turbulence level is calculated for different frequencies for optically thin and thick media. We find that turbulent velocities varies greatly for different damping mechanisms, reaching ~ 100 km s^{-1} for the collisional damping of small frequency waves.

Subject headings: accretion, accretion disks — magnetic fields — stars: pre-main-sequence — turbulence — waves

1. Introduction

The current picture of Classical T Tauri stars (CTTSs), the so called class II objects (Lada 1987), consists of a central young star, surrounded by a geometrically thin disk. Instead of a classical boundary layer connecting the disk directly to the star, as proposed by Lynden-Bell & Pringle (1974), the disk is disrupted by the star's magnetic field at a given radius. Accretion flow for smaller radii follows the star's magnetic field lines until it impacts on the stellar surface (Ghosh & Lamb 1979a,b; Königl 1991). This "magnetospheric accretion model" explains observational signatures seen in some CTTSs as, for example, the excess of optical and ultraviolet continuum flux (veiling) and redshift absorption features in the emission line profiles (inverse P Cygni profiles) (Muzerolle, Hartmann, & Calvet 1998; Hartmann, Hewett, & Calvet 1994, hereafter HHC). Low rotation rates, inferred from observations for CTTSs, are hard to explain by the classical boundary layer model. However, they can be explained in the magnetospheric accretion model.

Originally suggested by Ghosh & Lamb (1979a,b) for neutron stars, the magnetospheric accretion model was proposed to explain the hot spots observed in DF Tauri by Bertout, Basri & Bouvier (1988). Camenzind (1990) and Königl (1991) applied the original Ghosh-Lamb model to CTTSs. It is assumed, in this model, that the star has a dipole magnetic field. The basic idea behind this mechanism is that a sufficiently strong field can halt disk accretion at a given radius. At this radius, the magnetic pressure needs to be equal to the ram accretion pressure. For protostellar accretion disks, magnetic fields on the order of 1kG at the star's surface are sufficient to disrupt the disk. Magnetic fields of this magnitude are inferred from observations (Johns-Krull et al. 1999; Guenther et al. 1999). In order to follow the magnetic field lines, the gas needs to be coupled to the magnetic field. For CTTSs disks, this coupling is achieved if the temperatures at the truncation radius ($R \leq 0.1$ AU) are greater than 10^3 K since collisional ionization of metal atoms is then effective (Umebayashi & Nakano 1988). The truncation radius, R_{trun}, must be smaller than the co-rotation radius, R_{co}, in order for accretion to proceed. Contrary to observational evidences, for the case $R_{trun} < R_{co}$, the star should spin up. Wind models that possess open magnetic field lines have been proposed to explain the observed low rotation rates. However, the exact position (or region) of the truncation radius is still under debate (Camenzind 1990; Shu et al. 1994; Hartmann 1998). These open field lines carry off mass and angular momentum. Several CTTSs do, in fact, show P Cygni profiles in many lines, as well as in forbidden-line emission, indicating the presence of outflows. Some CTTSs are known to have jets (e.g., DG Tau, see Bacciotti et al. 2000).

HHC and more recently Muzerrole et al. (1998) calculated magnetospheric accretion models, solving radiative transfer equations in the Sobolev approximation, in order to obtain

theoretical Balmer line profiles. Profiles which are in reasonable agreement with observations were obtained. The calculated line profiles are slightly asymmetric, with blueshifted centroids, sometimes showing redshifted absorption components. However, Alencar & Basri (2000), analyzing spectra from 30 CTTSs, noted that only 20% of their sample showed inverse P Cygni profiles in the studied lines. They argued that winds, turbulence and rotation of the central star must be taken into account to fully explain the observations. Basri (1990) previously suggested that turbulence may be important in the formation of line profiles. Edwards et al. (1994) suggested that Alfvén waves can be the source of this turbulence. Also, Johns & Basri (1995), when analyzing the spectra of SU Aur, found that a turbulent velocity component at the base of a wind is necessary in order to fit the observed spectra.

The major uncertainty in the radiative magnetospheric model calculations is the temperature profile of the tube. Martin (1996, hereafter MA) calculated the energy balance of the gas. He included heating by adiabatic compression of the magnetic field lines, Balmer photoionization and ambipolar diffusion. However, the temperatures that he obtained are very low and cannot explain the observed line fluxes. Thus, an additional heating mechanism must take place in the tube.

Combining the evidence for turbulence and the necessity of an additional heating mechanism, we suggest that the heating by Alfvén waves is important in the magnetic flux tubes of CTTSs. We first study the possibility that the waves are generated at the star's surface due to the shock produced by the accreting matter, as suggested by Scheurwater & Kuijpers (1988). A model in which the waves are generated locally is then studied, following the same approximation used in our previous paper (Vasconcelos, Jatenco-Pereira & Opher 2000, hereafter, Paper I). Independent of the generation mechanism, we calculate the damping length for the waves, investigating four different damping mechanisms: 1) nonlinear; 2) turbulent (Paper I); 3) collisional; and 4) viscous-resistive (Osterbrock 1961). The associated heating rates and the degree of turbulence are calculated. We use a theoretical temperature profile, varying from ~ 7500 K to ~ 8300 K, which produces the observed line features.

Various damping mechanisms for Alfvén waves have been suggested in the literature, such as Alfvén resonant heating of solar loops; wave damping by phase mixing (also in the solar context); and cyclotron heating, occurring as an Alfvén wave travels down a magnetic field gradient until its frequency matches the decreasing ion cyclotron resonance (magnetic beach). In addition to the more conventional collisional and viscous-resistive Alfvén wave dampings, we concentrate on nonlinear and turbulent damping, which our group has investigated in: the solar wind (Jatenco-Pereira & Opher 1989a; Jatenco-Pereira, Opher & Yamamoto 1994); protostellar winds (Jatenco-Pereira & Opher 1989b); late-type giant stars (Jatenco-Pereira & Opher 1989c); Wolf-Rayet stars (dos Santos, Jatenco-Pereira & Opher

1993a,b); quasar clouds (Gonçalves et al. 1993a,a); and extragalactic jets (Gonçalves et al. 1993b).

In §(2), we outline the magnetospheric accretion model investigated. This accretion model is the same as that of HHC. The damping mechanisms used are discussed in §(3), where the heating rates, damping lengths and related time-scales are evaluated for a reasonable set of parameters. We discuss the generation source for the waves and calculate the required degree of turbulence in §(4). Finally, the conclusions of this work are summarized in §(5).

2. The magnetospheric accretion model

The equations of the magnetospheric accretion model describe a column of gas following the lines of a dipole magnetic field that connect the disk to the star. In this paper, the equations used are the same as those of HHC. A cylindrical coordinate system is adopted (see Fig. 1)[1]. The streamlines are described by the equation

$$r = r_m \sin^2\theta, \tag{1}$$

where θ is the angle between the z-direction and r, the radial distance from the center of the star. The constant r_m is the value of r for $\theta = \pi/2$. We can also define a cylindrical radius R, which is the projection of r in the plane $z = 0$. In this paper, all figures are shown as a function of the radius R.

The poloidal velocity, parallel to the field lines, is

$$\mathbf{v_P} = -v_p \left[\frac{3\sin\theta\cos\theta\hat{\mathbf{R}} + (2 - 3\sin^2\theta)\hat{\mathbf{z}}}{(4 - 3\sin^2\theta)^{1/2}} \right], \tag{2}$$

where $\hat{\mathbf{R}}$ and $\hat{\mathbf{z}}$ are unit vectors in the R and z directions and

$$v_p = \left[\frac{2GM_*}{R_*} \left(\frac{R_*}{r} - \frac{R_*}{r_m} \right) \right]^{1/2}, \tag{3}$$

where M_* is the mass of the star and R_* its radius. The density of the fluid is

[1]For more details, see HHC.

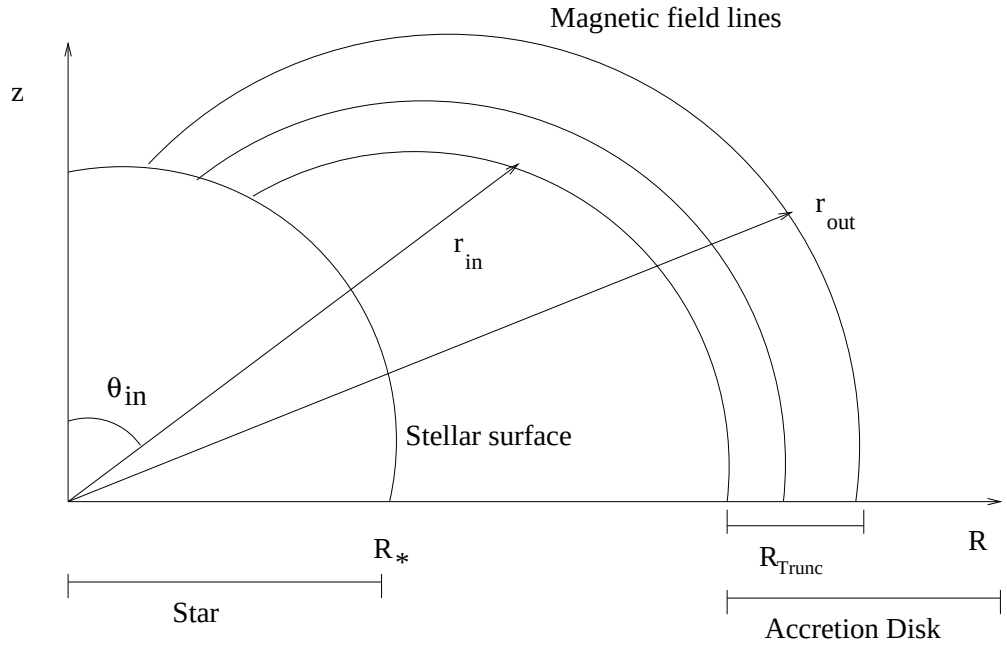

Fig. 1.— Sketch of the interface between the accretion disk and the star. The axis shows the cylindrical coordinates z (the vertical direction) and R (the projection of r in the plane $z = 0$). The star possesses a dipole magnetic field, which truncates the disk at the radius R_{trun}. The angle between the z-direction and the position vector r is θ. The inner and outer field lines are r_{in} and r_{out}, respectively. (For more details of the geometry, see HHC).

$$\rho = \frac{\dot{M}}{4\pi\left(\frac{1}{r_{in}} - \frac{1}{r_{out}}\right)} \frac{r^{-5/2}}{\sqrt{2GM_*}} \sqrt{\frac{4 - 3\sin^2\theta}{\cos^2\theta}}, \tag{4}$$

where $\dot{M}$ is the accretion rate and r_{in} and r_{out} the inner and outer field lines, respectively. A dipole magnetic field with intensity

$$B = \frac{m\sqrt{4 - 3\sin^2\theta}}{r^3}, \tag{5}$$

where m is the magnetic moment, is used.

It is not known what the exact temperature profile of the tube is. MA calculated the thermal structure of the gas funnel, but obtained values for the temperature that were too low to explain the observations. HHC adopted an ad hoc temperature profile that was able to reproduce the observations. In the absence of a reliable temperature estimate for the tube, we assume here a temperature profile similar to that of HHC, shown in Figure 2. The mean

temperature is ~ 8000 K. The temperature does not vary greatly inside the tube, dropping near the disk. As we show in the following sections, Alfvenic heating does not have a strong dependence on temperature and, thus, the exact profile is not of any great importance.

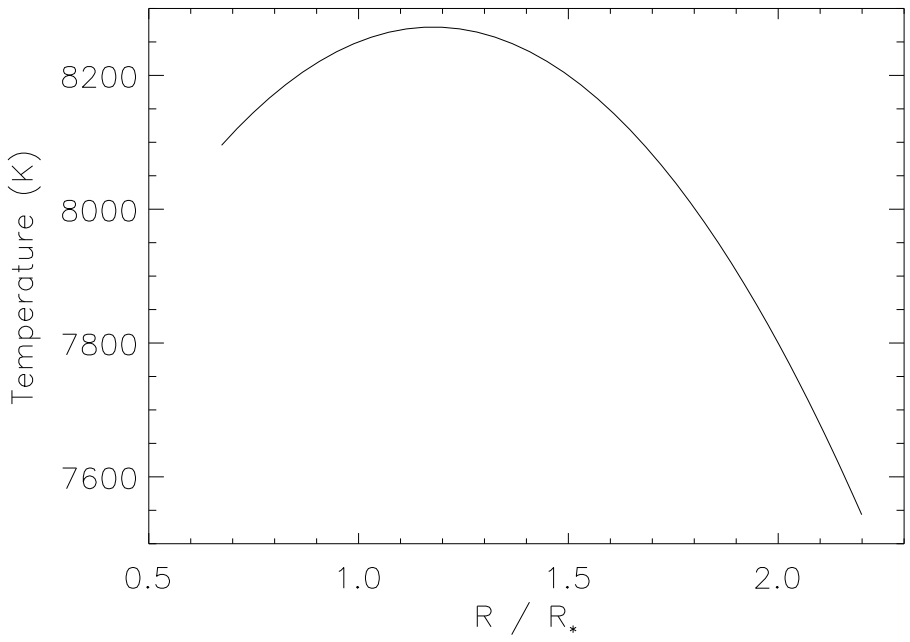

Fig. 2.— Temperature profile adopted in this work. The profile fits the observed line fluxes (e.g. Alencar & Basri 2000). The temperature near the star does not vary greatly, dropping near the disk. Since the Alfvenic heating does not have a strong dependency on temperature, the exact profile is not very important.

In Table 1, we show the magnetospheric model parameters adopted in our calculations, which are the same as those used by HHC.

3. Damping mechanisms

3.1. The damping lengths

When waves are generated in a non-ideal fluid, they are subject to dissipation mechanisms so that the energy carried by the wave is transferred to the fluid. We study four damping mechanisms in this work: 1) nonlinear; 2) turbulent; 3) collisional; and 4) viscous-resistive. In the nonlinear damping process, waves of large amplitudes interact and generate

compressive MHD waves which, in turn, decay into purely sonic modes. The damping rate associated with this mechanism is

$$\Gamma_{nl} = \frac{1}{4}\sqrt{\frac{\pi}{2}}\xi\varpi\left(\frac{c_s}{v_A}\right)\frac{\rho\langle\delta v^2\rangle}{B^2/8\pi}, \tag{6}$$

where ξ is a constant that can assume a value between 5-10, ϖ is the average angular frequency of the waves, c_s is the sound velocity, $v_A = B/\sqrt{4\pi\rho}$ is the Alfvén velocity, ρ and B are the fluid density and magnetic field, respectively, and $\langle\delta v^2\rangle^{1/2}$ is the velocity perturbation, which is a measure of the degree of turbulence of the system (Paper I).

The turbulent damping mechanism involves an energy cascade from large to small scales, in which microscopic processes dissipate the energy. The associated damping length is

$$L_T = L_{corr}v_A\langle\delta v^2\rangle^{-1/2}, \tag{7}$$

where $L_{corr}(\propto B^{-1/2})$ is the correlation length of the turbulent vortices (Hollweg 1986).

If the fluid is formed by two components, one ionized and the other neutral, wave damping, driven by collisions between the positive ions and the neutral particles (Osterbrock 1961) can occur. The e-folding length for the damping is

$$L_{coll} = \frac{v_A}{4\pi^2\nu^2}\frac{1+\eta}{\eta\tau_n}, \tag{8}$$

where ν is the average wave frequency, $\eta = \rho_H/\rho_i$ is the density contrast between the neutral and ionized particles, and τ_n, the mean collision time.

For a hydrogen fluid, the mean collision time (in seconds) is

$$\tau_n \approx 10^{12}T^{-1/2}n_H^{-1}, \tag{9}$$

where n_H is the neutral hydrogen particle density and T is the fluid temperature (Spitzer 1962). The wave frequency can be written in terms of the ion-cyclotron frequency, ω_i,

$$\nu = \frac{\varpi}{2\pi} = \frac{F\omega_i}{2\pi} = \frac{FeB}{2\pi m_i c}, \tag{10}$$

where F is a free parameter ($F < 1$ corresponds to low-frequency waves), e, m_i and c are the electron charge, ion (hydrogen) mass and the velocity of light, respectively.

Substituting (9) and (10) in equation (8) we obtain,

$$L_{coll} \approx v_A \left(\frac{m_i c}{FeB}\right)^2 \frac{n_H \sqrt{T}}{10^{12}} \frac{1+\eta}{\eta}. \tag{11}$$

Finally, we discuss the fourth damping mechanism which is related to the viscosity μ and to the finite electric conductivity (σ) of the gas. In this case, the e-folding length is,

$$L_{\sigma,\mu} = \frac{v_A^3}{4\pi^2 \nu^2 \left(\frac{c^2}{4\pi\sigma} + \frac{\mu}{\rho}\right)}. \tag{12}$$

The electric resistivity η_e for a partially ionized gas is (Spitzer 1962),

$$\eta_e = \frac{c^2}{4\pi\sigma} \approx 7.148 \times 10^{10} T^{-3/2}. \tag{13}$$

From Spitzer (1962), the viscosity for a gas composed mainly of hydrogen is

$$\mu \approx 2 \times 10^{-15} T^{5/2} \text{ g cm}^{-1} \text{ s}^{-1}. \tag{14}$$

Substituting equations (13) and (14) in equation (12), we obtain

$$\begin{aligned} L_{\sigma,\mu} &\approx \left(\frac{m_H c}{FeB}\right)^2 \\ &\times \frac{v_A^3}{\left(7.148 \times 10^{10} T^{-3/2} + \frac{2\times 10^{-15} T^{5/2}}{\rho}\right)}, \end{aligned} \tag{15}$$

where the F parameter is defined in equation (10).

3.2. Heating rates

As outlined in Paper I, heating rates are given by

$$H_A = \frac{\Phi_w}{L_A}, \tag{16}$$

where H_A is the heating rate associated with a generic damping mechanism, $\Phi_w = \rho \langle \delta v^2 \rangle v_A$ is the wave flux and L_A is the damping length. We derived the heating rates for both the nonlinear and turbulent damping mechanisms in Paper I. They are, respectively:

$$H_{nl} = \frac{\sqrt{2}}{8} f^4 F \frac{e\xi}{m_i c} \left(\frac{\gamma \Re}{\bar{m}}\right)^{1/2} (\rho T)^{1/2} B^2, \tag{17}$$

and

$$H_T \approx 2.985 \times 10^{-6} \frac{f^3 B^{7/2}}{\sqrt{\rho}}, \tag{18}$$

where we used the same parametrization as that of Paper I,

$$\langle \delta v^2 \rangle^{1/2} = f v_A, \tag{19}$$

and f is a free parameter. As noted above, $\langle \delta v^2 \rangle^{1/2}$ is a measure of the degree of turbulence of the flow. In equation (17), $\gamma = c_p/c_v$ is the ratio of the specific heats, $\Re$ is the gas constant, and $\bar{m}$, the mean molecular weight.

Using equation (19), the Alfvén wave flux can be written as,

$$\Phi_w = \rho f^2 v_A^3 = f^2 \frac{B^3}{\sqrt{(4\pi)^3 \rho}}. \tag{20}$$

The collisional heating rate is given by,

$$H_{coll} \approx 1 \times 10^{12} \left(\frac{fFe}{m_H c}\right)^2 \frac{B^4}{4\pi (n_p + n_H)\sqrt{T}}. \tag{21}$$

Equation (21) is derived from equations (11) and (16), using the definition of Φ_w. In this equation, n_p is the proton number density. Correspondingly, for the case when the damping is due to both viscosity and the resistivity of the fluid, the heating rate is

$$\begin{aligned} H_{\sigma,\mu} &\approx \rho \left(\frac{fFeB}{m_H c}\right)^2 \\ &\times \left(7.2 \times 10^{10} T^{-3/2} + \frac{2 \times 10^{-15} T^{5/2}}{\rho}\right). \end{aligned} \tag{22}$$

In order to calculate the heating rates and damping lengths described above, we set values for the variables, using the parameters of Table 1. We use the following values: $f = 0.004$ (justified in later sections), $F = 0.1$, $\xi = 5$, $m_i = m_H = 1.673 \times 10^{-24}$ g, $\gamma = 5/3$ and $\bar{m} = 0.613$ (Paper I). In order to obtain the ratio of protons to neutral atoms, we

solve the Saha equation for the values of the temperature and density given in Figure 2 and in equation (4), respectively. The obtained values are shown in Figure 3. In solving the damping lengths for the profiles described in §2 (equations 1 - 5 and Fig. 2), we use $r_m = r_{in} = 2.2R_\odot$ and 0.74 rad $\lesssim \theta \lesssim$ 1.57 rad. The results of the calculations are shown in Figures 4 and 5.

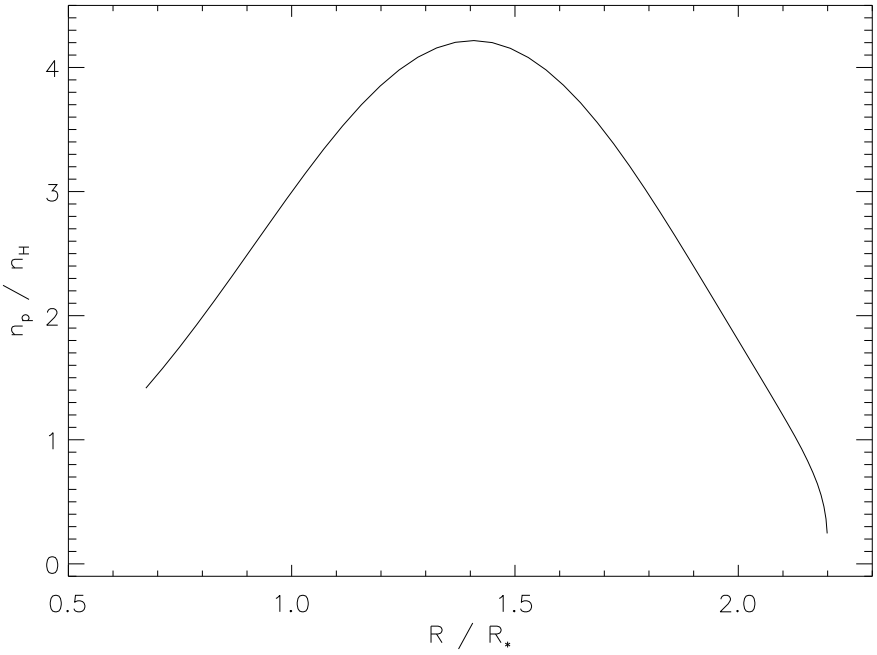

Fig. 3.— Ratio of protons to neutral atoms. We note that the ratio drops near the disk. This is because the temperature decreases there and the density increases. Near the star the ratio also drops, but not as dramatically as near the disk.

In Figure 4, we plot the heating rates for the adiabatic heating mechanism (MA) (Fig. 4a) and for the wave damping mechanisms (Fig. 4b), described by equations 17, 18, 21 and 22. It can be seen that the Alfvenic heating rates are larger than the adiabatic heating rate. Figure 5a shows that the damping lengths are small compared to the stellar radius. Thus, as soon as the waves are generated, they are rapidly damped. We note that the nonlinear damping length is much bigger than the other damping lengths.

In Figure 5b, we show the time-scales associated with each of the damping processes. For comparison, we estimate the time-scale associated with free-fall accretion:

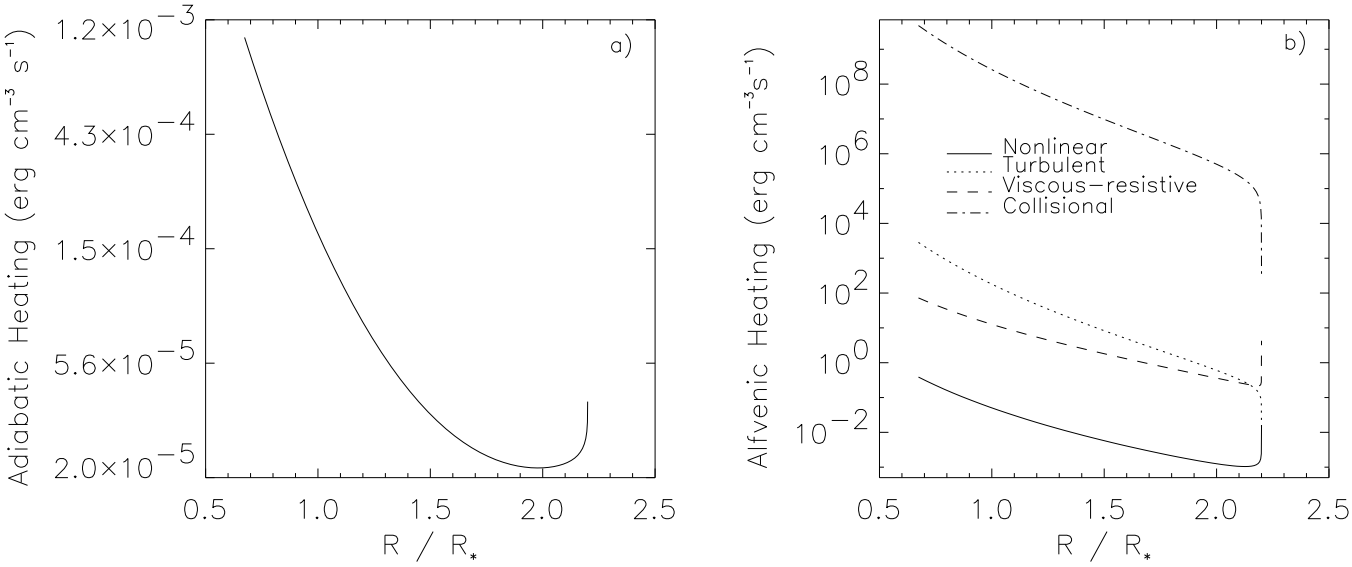

Fig. 4.— Heating rates (ergs cm^{-3} s^{-1}): 4a) Adiabatic, calculated according to MA; 4b) Alfvenic for nonlinear (solid line), turbulent (short-dashed line), viscous-resistive (long-dashed line) and collisional (dash-dotted line) damping mechanisms. We note that the heating rates vary from $\sim 10^{-2}$ to $\sim 10^{11}$ erg cm^{-3} s^{-1}.

$$t_{ff} \sim \frac{\Delta \mathrm{L}}{v_{ff}} \sim \frac{10^{12}}{3 \times 10^7} \sim 3.3 \times 10^4 \mathrm{s} \sim 9 \text{ hr}. \tag{23}$$

As can be noted, Alfvén waves are dissipated very quickly. Even the slowest damping-time (nonlinear) is 10^4 times shorter than the free-fall time.

4. Sources for Alfvén waves in magnetic accretion tubes

4.1. Generation of Alfvén waves at the star's surface

Scheurwater & Kuijpers (1988) proposed that, when the fluid in the accretion column shocks with the stellar surface, the resultant turbulence generates Alfvén waves. Thus, in a first approximation, we consider that the waves are generated only at the surface of the star. However, taking into account the results showed in Figure 5a, we note that the waves are dissipated locally. Therefore, unless thermal conduction is large, Alfvén waves cannot be considered an efficient heating mechanism for the tube, in this scenario. In order to determine whether the damping of Alfvén waves might be responsible for the increase of the

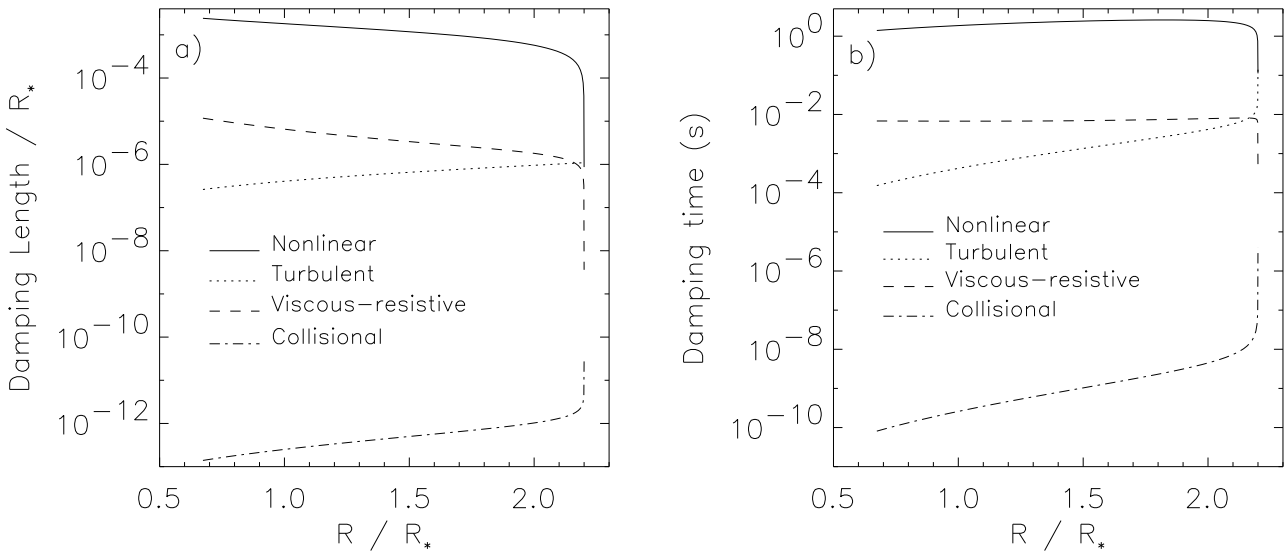

Fig. 5.— Damping lengths and time scales: 5a) Damping lengths calculated for the mechanisms described in section 3. The lengths are divided by the stellar radius. We note that the lengths are very small, compared to the stellar radius. Thus we can assume that as soon as the waves are generated, they are rapidly damped. (For more discussion, see text). 5b) Time-scales related to nonlinear (solid line), turbulent (short-dashed line), viscous-resistive (long-dashed line) and collisional (dash-dotted line) damping mechanisms. The time-scales vary from $\approx 10^{-10}$ s for the collisional mechanisms to ≈ 3 s for the nonlinear mechanism. Even the slowest time-scale is very short, compared to the free-fall time-scale which is ≈ 9 hr.

temperature in the tube in this model, we estimate the thermal conductivity near the star.

For an incompressible fluid (with $\rho \sim$ constant), the change in temperature with time is given by the thermal conduction equation,

$$\frac{\partial T}{\partial t} = -\mathbf{v} \cdot \nabla T + \frac{\kappa}{\rho c_v} \nabla^2 T - \frac{1}{c_v} \mathcal{L}(\rho, T), \tag{24}$$

where κ is the thermal conductivity coefficient, c_v is the specific heat at constant volume, and $\mathcal{L}(\rho, T) = \Gamma - \Lambda$, the energy loss rate. Here, Γ represents the energy gains and Λ, the energy losses. In this work, we assume that $\mathcal{L}$ is approximately zero. Thus, the energy gains are balanced by energy losses (Shu 1992).

In order to estimate the relative importance of thermal conduction in magnetic flux tubes, we divide the first term by the second term on the right hand side of equation (24).

This gives

$$\frac{|-\mathbf{v}\cdot\nabla T|}{\frac{\kappa}{\rho c_v}\nabla^2 T} \sim \left(\frac{\rho c_v}{\kappa}\right) v\Delta \mathrm{L}. \tag{25}$$

The specific heat at constant volume for a non relativistic, non degenerate, monoatomic ideal gas is

$$\frac{c_v}{\mathcal{M}} = \frac{3k}{2m}, \tag{26}$$

where $\mathcal{M}$ is the molecular weight and k is Boltzmann's constant. ¿From Spitzer (1962), the thermal conductivity coefficient is

$$\kappa \approx 2\times 10^{-4}\frac{T^{5/2}}{Z^4 \ln\Lambda}, \tag{27}$$

where Z is the particle charge and $\ln\Lambda$ is the Coulomb logarithm.

Substituting equations (26) and (27) in equation (25), we obtain

$$\frac{|-\mathbf{v}\cdot\nabla T|}{\frac{\kappa}{\rho c_v}\nabla^2 T} \sim \frac{3\,n\,k\times 10^4}{4}\frac{v\,\Delta \mathrm{L}\ln\Lambda}{T^{5/2}}. \tag{28}$$

The Λ parameter is given by

$$\Lambda \sim 1.3\times 10^4 \frac{T^{3/2}}{n_e^{1/2}}, \tag{29}$$

where n_e is the electron density. We assume free-fall velocities on the order of 300 km s^{-1}, densities and electron densities of about 10^{12} cm^{-3} and 5×10^{11} cm^{-3}, respectively, and temperatures around 8000 K (Muzerrole et al. 1998). The length of the tube is approximately 10^{12} cm. Using these values in equation (28), we obtain

$$\frac{|-\mathbf{v}\cdot\nabla T|}{\frac{\kappa}{\rho c_v}\nabla^2 T} \sim 5\times 10^{10}. \tag{30}$$

Therefore, the term related to thermal conductivity, $(\kappa/\rho c_v)\nabla^2 T$, is very small, compared to the term $|-\mathbf{v}\cdot\nabla T|$. We thus conclude that temperature gradients are maintained in the tube because thermal conduction is not efficient. Estimating the time scale related to this process, we obtain

$$t_{therm} \sim \frac{\rho c_v}{\kappa}(\Delta \mathrm{L})^2 \sim 5.5 \times 10^7 \text{ years.} \quad (31)$$

This time scale is very long, compared to the free fall time scale ($t_{ff} \sim 9$ hr). We conclude, therefore, that thermal conduction is not important for the region near the star and, consequently, Alfvén waves generated near the shock region cannot contribute to an increase in temperature of the whole tube.

4.2. Generation of Alfvén waves in the tube

Jafelice et al. (1990, and references therein) proposed that the Kelvin-Helmholtz (K-H) instability produced in an extragalactic jet by the shear in the plasma flow with respect to the ambient medium can generate MHD waves. They suggested that these waves, once damped, can give rise to currents capable of generating magnetic fields. In the case of the magnetic funnels of T Tauri stars, there is also a shear between the gas falling onto the star and the external medium. This flow, however, is sub-Alfvénic and, therefore, the development of Kelvin-Helmholtz modes is not expected. In fact, Hardee et al. (1992) performed an analytical and numerical analysis of the Kelvin-Helmholtz instability in magnetized jets and show that the fundamental mode is completely stabilized if the magnetic Mach number $[M_{ms} = v_{tube}/\sqrt{c_s^2 + v_A^2}]$ is less than unity.

However, they also find that for some magnetosonic mach numbers the reflection mode is excited. There are two ranges shown in their Figure 1 where this can happen: $0.4 \leq M_{ms} \leq 0.45$ and $M_{ms} \geq 0.9$. In Figure 6, we plot magnetosonic Mach numbers obtained for the parameters of the tube. We see that two regions can support reflection modes of the K-H instability: one, near the star, extends from $0.705R_*$ to $0.780R_*$. The other region, near the disk, extends from $1.58R_*$ to $1.90R_*$, where $M_{ms} \geq 0.9$. Thus, we see that Alfvén waves can be generated in two regions in the tube.

We can also generate turbulence if the accretion is variable. In this case, there will be shocks inside the tube, which can perturb the environment. Indications for variable accretion have come from different sources, for example, the internal knots observed in protostellar jets (for a recent review of both theory and observations of Herbig-Haro jets, see Reipurth & Raga 1999). Sano & Miyama (1999) made numerical simulations of weakly ionized, magnetized accretion disks and found that a magnetorotational instability (for a review, see Balbus & Hawley 1998) acts beyond 15 AU. The infalling matter accumulates in the region ~ 15 AU and a gravitational instability may be important in transporting the flow to smaller radii. Even if a larger region of the disk may be made susceptible to the action of the

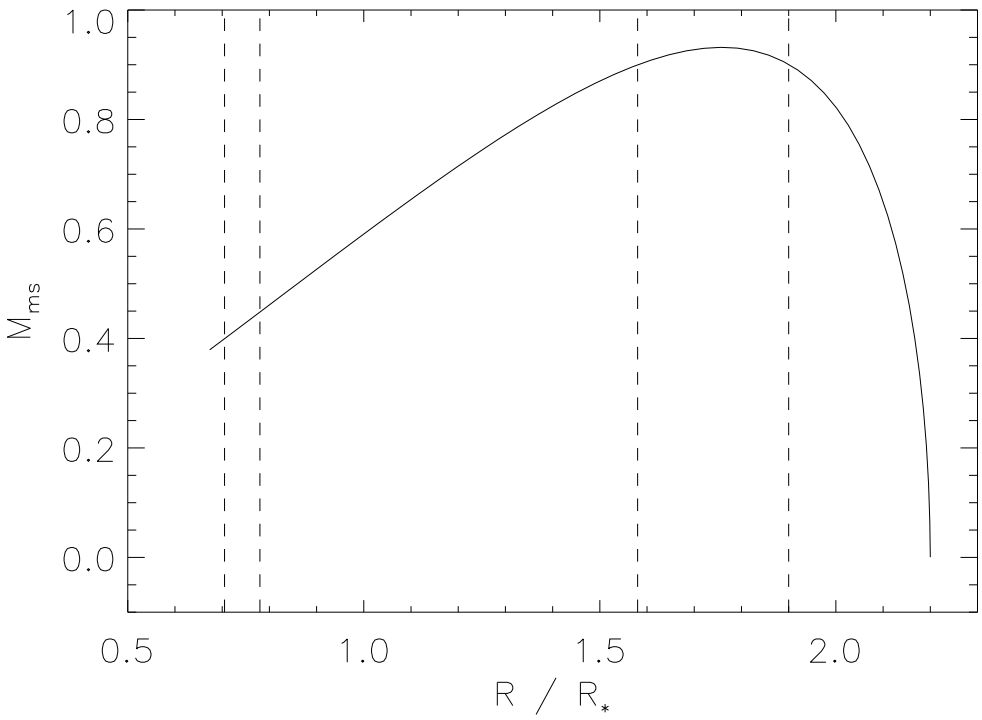

Fig. 6.— Magnetosonic Mach numbers for the tube. The values varies from 5×10^{-4} to 0.9. The vertical dashed lines mark where in the tube the conditions for the development of the K-H reflection modes hold. There are two regions, one near the star where $0.705 \leq R/R_* \leq 0.78$ and the other near the disk, where $1.58 \leq R/R_* \leq 1.9$.

magnetorotational instability due to ionization by cosmic rays (Gammie 1996) or X-rays from the central star (Igea & Glassgold 1999) or by the damping of Alfvén waves (Paper I), it is likely that there is some region where the magnetorotational instability cannot occur (Gammie 1996) and a gravitational instability probably occurs allowing accretion to smaller radii.

There is no consensus about the position of the truncation radius, R_{trun}, (Hartmann 1998). The interaction of the star's magnetic field with the accretion disk can be highly dynamic, so that, changes in the position of R_{trun} can occur (Safier 1998). This would give rise to variable accretion. Johns & Basri (1995), analyzing the line profile variability of SU Aurigae, argue that variation of the red absorption feature in Hβ is evidence for unsteady accretion.

The possibility of a turbulent component in accretion tubes has been proposed by a

number of people. Basri (1990) suggested that wings of Balmer lines are formed in a turbulent region near the star. Edwards et al. (1994) suggested that Alfvén waves could be the source for such a turbulence and Johns & Basri (1995) reproduced some symmetric Balmer lines profiles by adding turbulent velocity components at the base of an expanding wind.

Taking all this evidence into account, we suggest that Alfvén waves are generated in the tube. In this paper we do not address the problem related to the excitation of the Alfvén waves generated in a turbulent medium. Instead, we use results from previous theoretical, solar wind and laboratory findings.

A magnetized, perturbed environment excites MHD modes, in particular, the Alfvenic mode. For example, laboratory plasma experiments (Burke, Maggs, & Morales 1998) show excitation of Alfvén modes with frequencies around $0.1\Omega_i$, where Ω_i is the ion-cyclotron frequency. The frequency spectrum is seen to obey a Kolmogorov distribution. A frequency spectrum of Alfvén waves generated by turbulence could be a Kolmogorov one. Moreover, radio-wave scintillation observations of the ionized interstellar medium show a density fluctuation spectrum that approximately obeys a Kolmogorov distribution (Armstrong, Rickett & Spangler 1995; Lithwick & Goldreich 2001), i.e. the fluctuations are approximately proportional to $\lambda^{1/3}$, where lambda is the size of the density fluctuation. Recent theories and simulations on MHD turbulence confirm the Kolmogorov spectrum for Alfvén waves (Goldreich & Sridhar 1995, 1997; Lithwick & Goldreich 2001; Maron & Goldreich 2001). Lithwick & Goldreich (2001) extended the work of Goldreich & Sridhar (1995, 1997) which treated incompressible MHD turbulence, to include the effects of compressibility and particle transport. They calculated small-scale density spectra in turbulent interstellar plasmas. They also considered compressible turbulence in plasmas with β less than unity that match those found in the magnetic tubes of T Tauri stars. They argued that the dynamics of the cascade is roughly independent of β. In the above mentioned papers, it was assumed that MHD wave-packets propagate at the Alfvén speed, in a direction either parallel or antiparallel with respect to the local mean magnetic field and that the nonlinear interactions are restricted to collisions between oppositely directed wave-packets. Maron & Goldreich (2001) made simulations of the interaction between oppositely directed Alfvén waves.

In our previous paper (Paper I), instead of a wave spectrum, we assumed a mean frequency, $\varpi = Fw_i$, while in this paper, we treat different frequency values. The wave frequency obtained from laboratory experiments (e.g., Burke et al. 1998), $\Omega_{sup} \sim 0.1\Omega_i$, could be taken as the upper limit for the wave spectrum. On the other hand, Scheurwater & Kuijpers (1988) showed that Alfvén wave frequencies can be greater than $10^{-5}\Omega_i$. We, therefore, study the frequency interval $10^{-5}\Omega_i \leq \Omega \leq 0.1\Omega_i$. Assuming this frequency spectrum, we calculate the damping lengths and corresponding $f = \langle \delta v^2 \rangle^{1/2}/v_A$ parameter for

all the damping mechanisms treated in section 3. Thus, hereafter, f is not a free parameter anymore. We assume that the energy released by the damping of the Alfvén waves in a given volume is radiated away. Thus, we have

$$\int_V H_{nl,T} dV = \tau \sigma T^4 A, \tag{32}$$

where T is given by Figure 2, τ is the optical depth, σ is the Stefan-Boltzmann constant, and A, the area. For a given τ and temperature profile, we know the amount of energy that is radiated away. This must be equal to the energy dissipated by the Alfvén waves, which is determined by f and the damping mechanism used.

Figure 7 shows the results of our calculations, which were made for three different values of the optical depth τ and for $10^{-5} \leq F \leq 0.1$. Since the star is not strongly obscured by the tube, it is likely that the mean optical depth is less than 1. Taking into account the values of the adiabatic heating (Martin 1996) and calculating the associated optical depth, we obtain $\tau \sim 10^{-3}$. However, for the sake of completeness, we made the calculations for $\tau = 10^{-2}$ and $\tau = 1$ as well. Figure 7 shows the damping lengths divided by the length of the tube, calculated according to equation (32), for the nonlinear and turbulent damping mechanisms mentioned above.

The left column of Figure 7 shows the nonlinear damping lengths. We note that even for $\tau = 10^{-3}$ with the lowest frequency ($F = 10^{-5}$), the damping length is less than the tube length. This implies, as seen in section 4.1, that the nonlinear damped waves cannot heat the whole tube if they are formed only at the surface of the star. The same conclusion applies to turbulent damping (right column of Figure 7). According to equations (6) and (32), the dependency of the nonlinear damping length on the optical depth is $L_{nl} \propto \tau^{-1/2}$, the same as for frequency, $L_{nl} \propto F^{-1/2}$. For the turbulent damping, there is no dependency on frequency, whereas $L_{tur} \propto \tau^{-1/3}$ (equations 7 and 32).

Figure 8 shows the damping lengths for the collisional and viscous-resistive damping, divided by the tube length. The collisional damping lengths are plotted in the left column and, in the right column, we plot the results for the viscous-resistive mechanism. As noted for the nonlinear and turbulent cases, damping lengths for the collisional mechanism are smaller than the tube length, for all frequencies considered. Thus, waves formed at the surface of the star undergoing collisional damping cannot heat the whole tube. The only mechanism that might be able to heat the tube entirely is viscous-resistive damping. If the wave frequency is lower than $10^{-4}\Omega_i$, the viscous-resistive damping length is comparable to the tube length, regardless of the optical depth. We note that for collisional damping, the variation of the damping length with frequency is very large, with L_{coll} ranging from $\approx 10^{-14}$

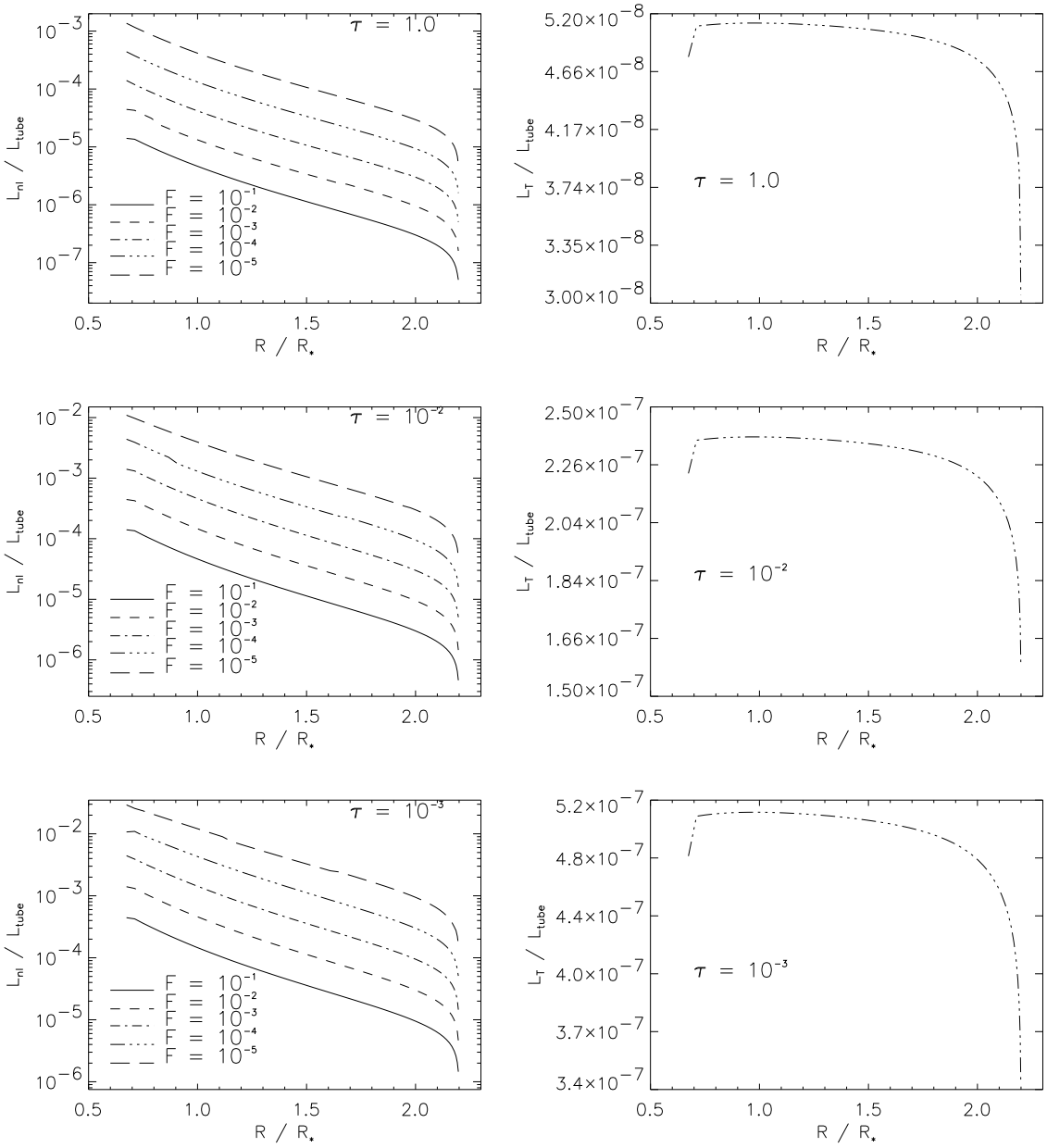

Fig. 7.— Variation of the damping lengths with tube position. The damping lengths are divided by the tube length. Each column shows the damping lengths related to one damping mechanism as a function of the wave frequency and the optical depth. The left column shows the nonlinear damping length; the right, the turbulent damping length. Optical depth decreases from top to bottom ($\tau = 1.0, 10^{-2}$ and 10^{-3}).

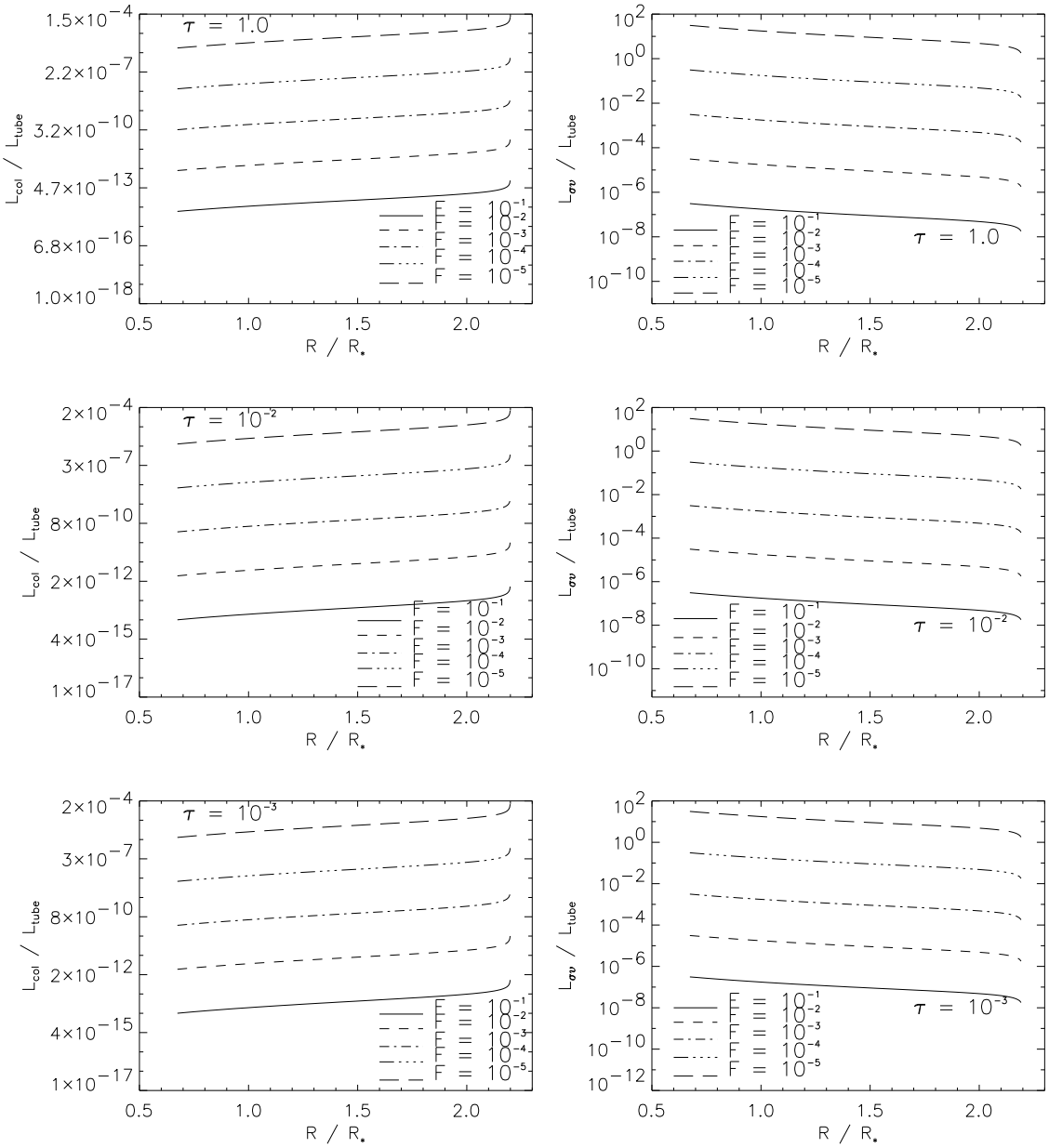

Fig. 8.— Damping lengths *versus* tube position as a function of wave frequency and optical depth. The damping lengths are divided by the tube length. In each pannel, different lines correspond to different wave frequencies, that range from $0.1\Omega_i$ to $10^{-5}\Omega_i$. The results for waves undergoing collisional damping are plotted in the left column. Viscous-resistive damping lengths are showed in the right column. Optical depths decreases from top to bottom.

for $F = 0.1$ to $\approx 10^{-6}$, for $F = 10^{-5}$, near the star, although variations with optical depth are almost negligible. In this case, a slight variation in frequency causes a large variation in the damping length. However, it is necessary to have frequencies well bellow $10^{-5}\Omega_i$ in order that the damping length be comparable to the length of the tube.

For viscous-resistive mechanism, the damping length also varies greatly with frequency (about 7 orders of magnitude near the star) and again the dependency with optical depth is weak. For waves with frequencies less than $10^{-4}\Omega_i$, the damping length is approximately equal the length of the tube.

Thus, we note a great variation of damping lengths with wave frequency for all mechanisms, except for the case of turbulent damping. In general, the lower the frequency, the larger the damping lengths.

Figure 9 shows the f parameter for nonlinear (left column) and turbulent damping (right column) mechanisms. In Figure 10, the calculations are for collisional (left column) and viscous-resistive damping (right column). The same analysis previously made for the damping lengths also applies here. In general, in order to fit the observations, a higher degree of turbulence is necessary if the gas is optically thick, even for the collisional and viscous-resistive mechanisms, although for the nonlinear and turbulent damping the dependency with optical depth is stronger. Again, the value of f varies greatly with frequency.

We can also analyze the values of the root mean square velocity, $\langle \delta v^2 \rangle^{1/2}$ which, according to equation (19) can be given in terms of the parameter f and the Alfvén speed. The results are shown in Figures 11 and 12, where the rms velocity is given in kilometers per second.

The left column of Figure 11 shows $\langle \delta v^2 \rangle^{1/2}$ for the nonlinear case, for three different optical depths. The value of $\langle \delta v^2 \rangle^{1/2}$ for the turbulent damping is shown in the right column of Figure 11. In Figure 12 we plot the rms velocity for the collisional and viscous-resistive mechanisms in the left and in the right columns, respectively. We find that the greater the optical depth, the greater the rms velocity, which increases with decreasing wave frequency. For the nonlinear and collisional mechanisms, the rms velocity can be as great as 60 km s^{-1} for an optically thick medium and a very low wave frequency ($F = 10^{-5}$). The $\langle \delta v^2 \rangle^{1/2}$ is smallest for the case of the viscous-resistive mechanism.

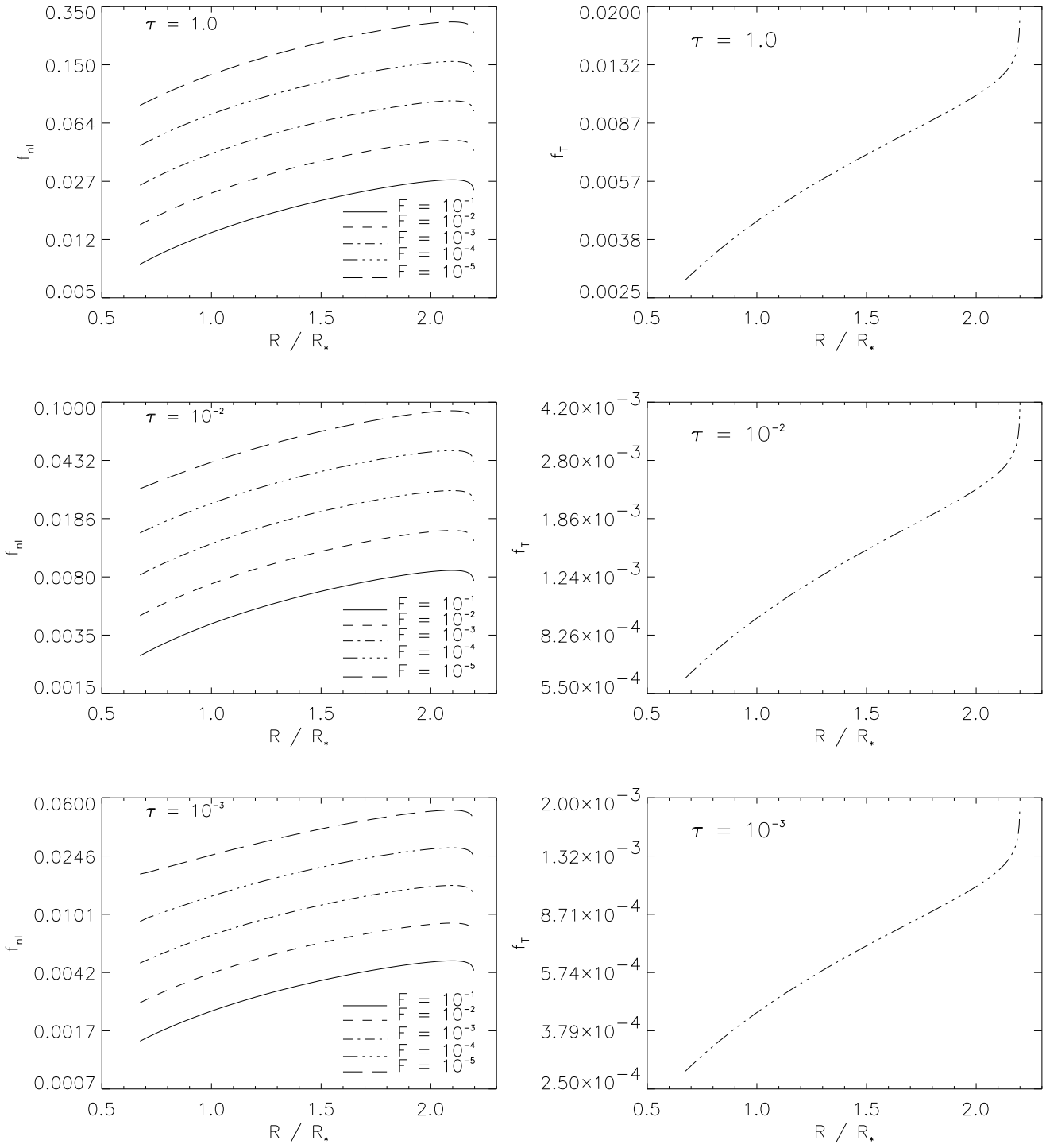

Fig. 9.— Degree of turbulence $f \equiv \langle \delta v^2 \rangle^{1/2} / v_A$. Each pannel correspond to a different optical medium. Also, different lines in the pannels correspond to different wave frequencies. The column sequency is: nonlinear damping (left) and turbulent damping (right).

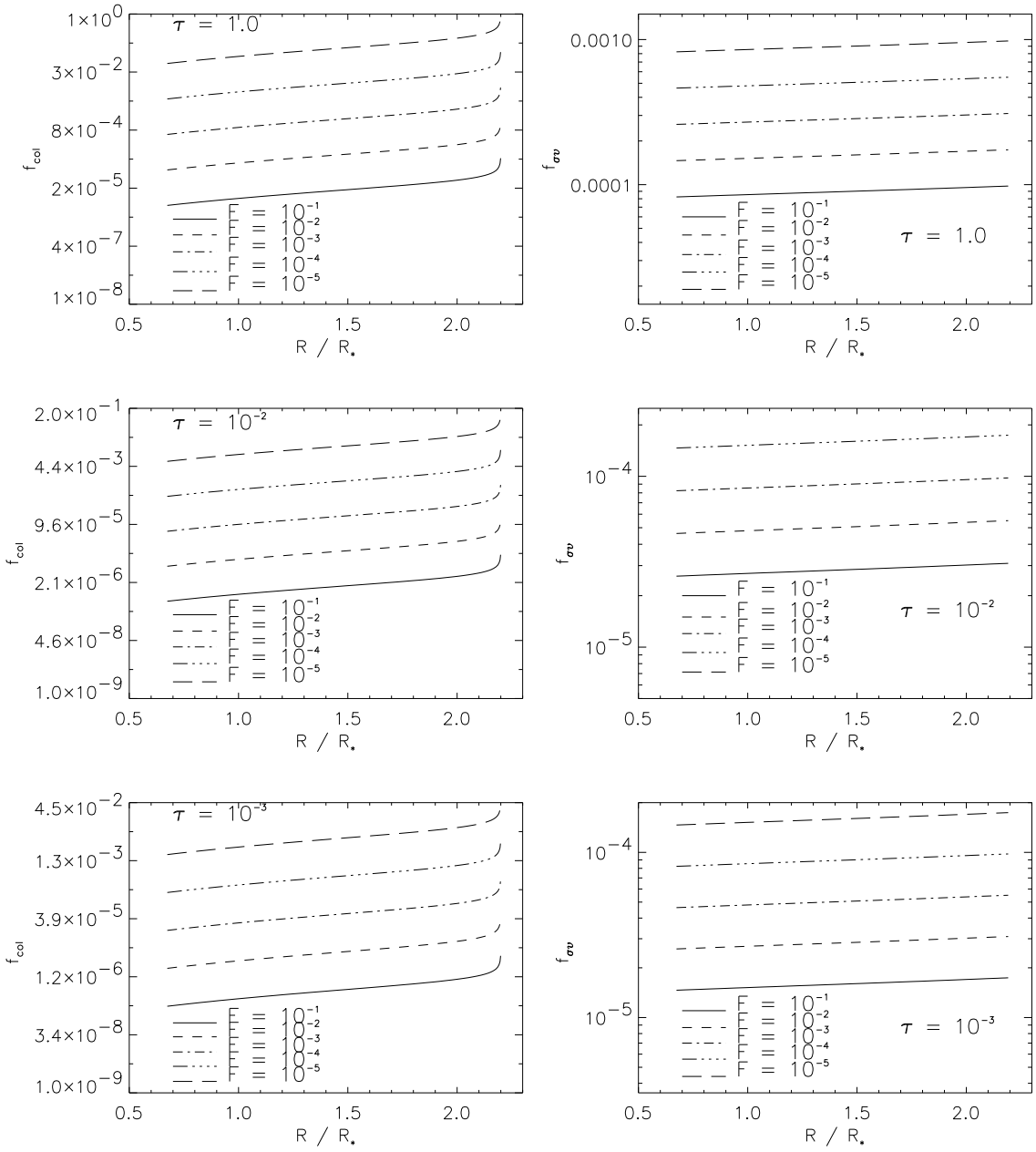

Fig. 10.— Parameter $f \equiv \langle \delta v^2 \rangle^{1/2} / v_A$. Each pannel correspond to a different optical medium. Also, different lines in the pannels correspond to different wave frequencies. In the left column are showed the results obtained for collisional damping mechanism and in the right column, the results for viscous-resistive damping.

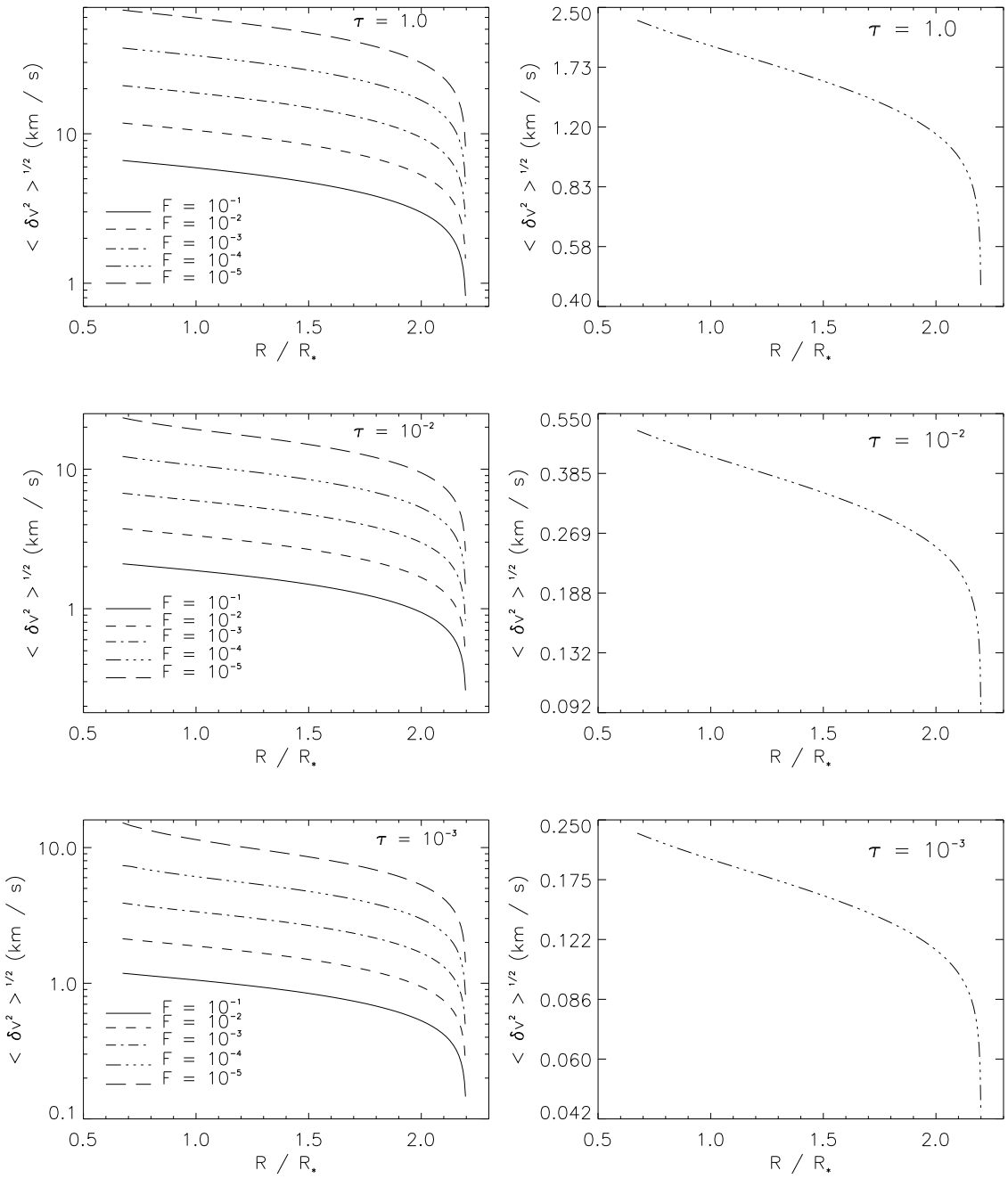

Fig. 11.— The root mean square velocity $\langle \delta v^2 \rangle^{1/2}$, given in kilometers per second. Each pannel correspond to a different optical medium. Also, different lines in the pannels correspond to different wave frequencies. Nonlinear damping: left column; turbulent damping: right column.

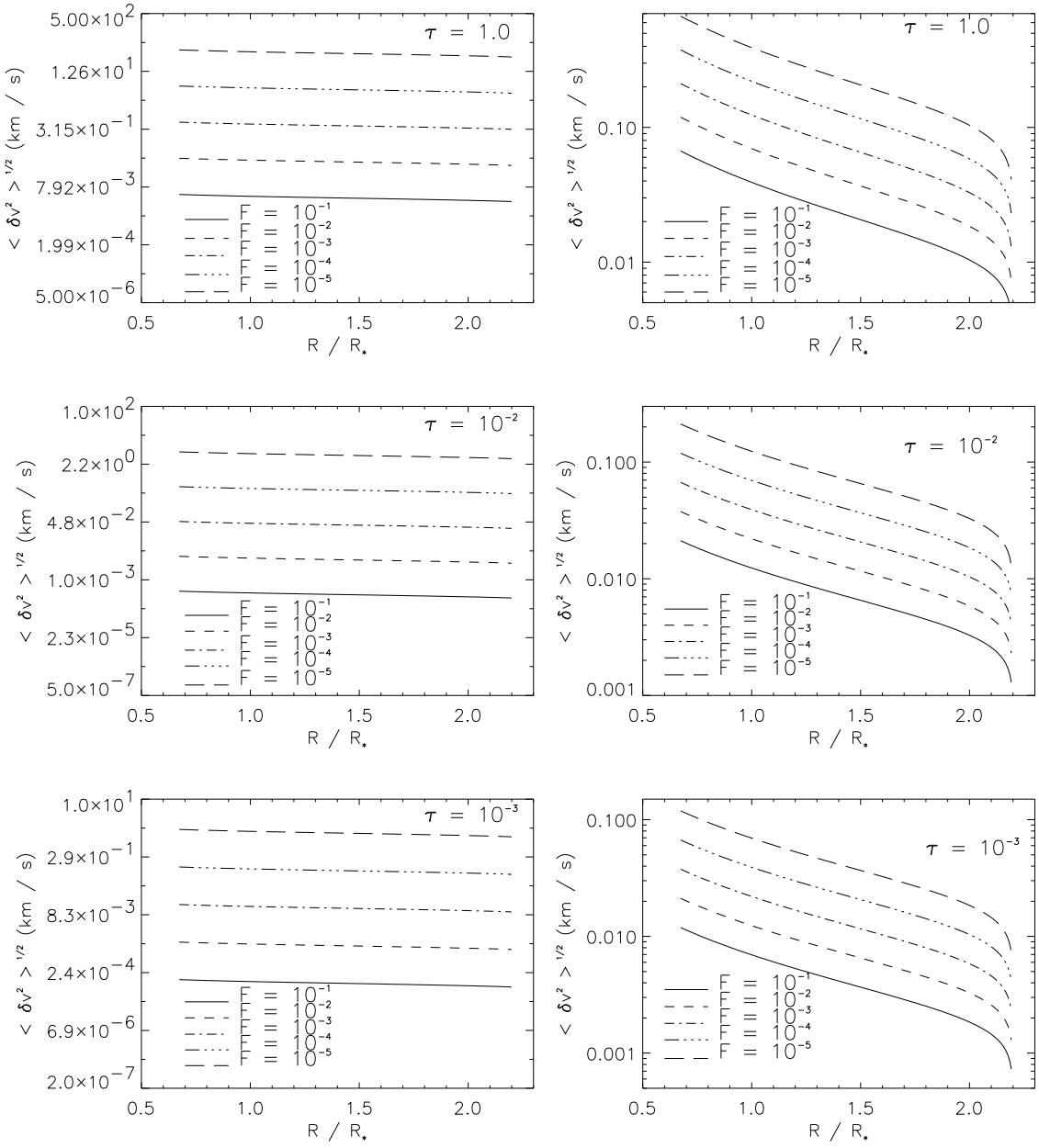

Fig. 12.— The root mean square velocity $\langle \delta v^2 \rangle^{1/2}$, given in kilometers per second. Each pannel correspond to a different optical medium. Also, different lines in the pannels correspond to different wave frequencies. Velocities obtained using the collisional mechanism are showed in the left column; velocities obtained for viscous-resistive damping are plotted in the right column.

5. Conclusions

In this work, we evaluated the role of damped Alfvén waves in the heating of the tubes in magnetospheric accretion models. We analyzed four damping mechanisms: 1) nonlinear; 2) turbulent; 3) viscous-resistive; and 4) collisional.

Using the values f = 0.004 and F = 0.1, all the damping lengths are found to be small compared with the length of the tube. Since our calculations show that the thermal conductivity of the gas is very small, these high-frequency waves, if generated only at the surface of the star, cannot heat the whole tube.

Extending the frequency range of the Alfvén waves from F = 0.1 to 10^{-5}, we found that the damping lengths varied strongly with frequency, spanning eight orders of magnitude for collisional damping. The parameter f was eliminated, imposing the constraint that the Alfvenic heating was converted into radiation in different optical media. The damping lengths were found to be much smaller than the tube length, except when the lowest frequency waves had viscous-resistive damping. In this case, the damping length was greater than the tube. If this were the dominant mechanism, Alfvén waves generated at the surface of the star could heat the whole tube. For the other cases, waves produced locally are required to explain the observations. The degree of turbulence $\langle \delta v^2 \rangle^{1/2}$ necessary to heat the tube was constrained, taking into account the optical depth of the gas. The larger the optical depth, the greater the degree of turbulence required. We found that the turbulent velocity of the Alfvén waves can reach 100 km s^{-1}, for very low frequency waves ($F = 10^{-5}$) undergoing collisional damping.

The authors thank an anonymous referee for useful suggestions. MJV would like to thank Adriano H. Cerqueira, Silvia H. P. Alencar and Bruno V. Castilho for very useful discussions and suggestions. MJV also thanks the Brazilian agency FAPESP (Proc. No. 96/00677-3) and PROPP/UESC for finantial support. VJP and RO thank the federal Brazilian agency CNPq for partial support. The authors would also like to thank the project PRONEX (41.96.0908.00) for partial support.

REFERENCES

Alencar, S. H. P. & Basri, G. 2000, AJ, 119, 1881

Armstrong, J. W., Rockett, B. J., & Spangle, S. R. 1995, ApJ, 443, 209

Bacciotti, F., Mundt, R., Ray, T. P., Eislöffel, J., Solf, J., & Camenzind, M. 2000, ApJ, 537, 49

Balbus, S. A., & Hawley, J. F. 1998, Rev. Mod. Phys., 70, 1

Basri, G. 1990, Mem. Soc. Astron, Ital., 61, 707

Bertout, C., Basri, G., and Bouvier, J. 1988, ApJ, 330, 350

Camenzind, M. 1990, Reviews in Modern Astronomy, Vol. 3 (Berlin: Springer), 234

dos Santos, L. C., Jatenco-Pereira, V. & Opher, R. 1993a, A&A, 270, 345

dos Santos, L. C., Jatenco-Pereira, V. & Opher, R. 1993b, ApJ, 410, 732

Edwards, S., Hartigan, P., Ghandour, L., & Andrulis, C. 1994, AJ, 108, 1056

Gammie, C.F. 1996, ApJ, 457, 355

Ghosh, P., & Lamb, F. K. 1979a, ApJ, 232, 259

Ghosh, P., & Lamb, F. K. 1979b, ApJ, 234, 296

Goldreich, P., & Sridhar, S. 1995, ApJ, 438, 763

Goldreich, P., & Sridhar, S. 1997, ApJ, 485, 680

Gonçalves, D. R, Jatenco-Pereira, V. & Opher, R. 1993a, ApJ, 414, 57

Gonçalves, D. R, Jatenco-Pereira, V. & Opher, R. 1993a, A&A, 279, 351

Gonçalves, D. R, Jatenco-Pereira, V. & Opher, R. 1996, ApJ, 463, 489

Guenther, E. W., Lehmann, H., Emerson, J. P., and Staude, J. 1999, A&A, 341, 768

Hardee, P. E., Cooper, M. A., Norman, M. L., & Stone, J. M. 1992, ApJ, 399, 478

Hartmann, L., Hewett, R., & Calvet, N. 1994, ApJ, 426, 669 (HHC)

Hartmann, L. 1998, Accretion Processes in Star Formation (Cambridge University Press)

Hollweg, J. V. 1986, J. Geophys. Res., 91, 4111

Igea, J., & Glassgold, A. E. 1999, ApJ, 518, 848

Jafelice, L. C., Opher, R., Assis, A. S., & Busnardo-Neto, J. 1990, ApJ, 348, 61

Jatenco-Pereira, V. & Opher, R. 1989a, ApJ, 344, 513

Jatenco-Pereira, V. & Opher, R. 1989a, MNRAS, 236, 1

Jatenco-Pereira, V. & Opher, R. 1989c,

Jatenco-Pereira, V., Opher, R. & Yamamoto, L. C. 1994, ApJ, 432, 409

Johns, C. M. & Basri, G. 1995, ApJ, 449, 341

Johns-Krull, C. M., Valenti, J. A., Hatzes, A. P., & Kanaan, A. 1999, ApJ, 501, L41

Königl, A. 1991, ApJ, 370, L39

Lada, C. J. 1987, in IAU Symposium 115, Star Forming Regions, eds. M. Peimbert and J. Jugaku (Dordrecht: Reidel), 1

Lithwick, Y., & Goldreich, P. 2001, astro-ph/0106425

Lynden-Bell, D., & Pringle, J. E. 1974, MNRAS, 271, 587

Maron, J., & Goldreich, P. 2001, ApJ, 554, 1175

Martin, S. 1996, ApJ, 470, 537 (MA)

Burke, A. T., Maggs, J. E., & Morales, G. J. 1998, Phys. Rev. Lett., 81, 3659

Muzerolle, J., Hartmann, L., & Calvet, N. 1998, ApJ, 492, 743

Osterbrock, D. E. 1961, ApJ, 134, 347

Reipurth, B., & Raga, A.C. 1999, The Origin of Stars and Planetary Systems, Eds. C.J. Lada & N.D. Kylafis (Kluwer Academic Publishers), 267

Safier, P. 1998, ApJ, 494, 336

Sano, T. & Miyama, S. M. 1999, ApJ, 515, 776

Scheurwater, R., & Kuijpers, J. 1988, A&A, 190, 178

Shu, F. 1992, Physics of Astrophysics: II. Gas Dynamics, (California: University Science Books)

Shu, F., Najita, J., Ostriker, E., Wilkin, F., Ruden, S. & Lizano, S. 1994, ApJ, 429, 781

Spitzer, L., Jr. 1962, Physics of Fully Ionized Gases (New York: Interscience-Wiley)

Umebayashi, T., & Nakano, T. 1988, Prog. Theor. Phys. Suppl., 96, 151

Vasconcelos, M. J., Jatenco-Pereira, V., & Opher, R. 2000, ApJ, 534, 967 (Paper I)

Table 1. Parameters of the magnetospheric model.

Parameter	Value
M_*	$0.8\ M_\odot$
R_*	$2\ R_\odot$
$\dot{M}$	$10^{-7}\ M_\odot\ yr^{-1}$
r_{in}	$2.2\ R_\odot$
r_{out}	$3\ R_\odot$
m[a]	4.38×10^{36} erg G^{-1}

[a]This value was obtained by assigning a value of 1 kG to the magnetic field at the surface of the star.